



Strathprints Institutional Repository

McArthur, Duncan and Hourahine, Benjamin and Papoff, Francesco (2014) Evaluation of E. M. fields and energy transport in metallic nanoparticles with near field excitation. Physical Science International Journal, 4 (4). pp. 564-575. , <http://dx.doi.org/10.9734/PSIJ/2014/7549>

This version is available at <http://strathprints.strath.ac.uk/46439/>

Strathprints is designed to allow users to access the research output of the University of Strathclyde. Unless otherwise explicitly stated on the manuscript, Copyright © and Moral Rights for the papers on this site are retained by the individual authors and/or other copyright owners. Please check the manuscript for details of any other licences that may have been applied. You may not engage in further distribution of the material for any profitmaking activities or any commercial gain. You may freely distribute both the url (<http://strathprints.strath.ac.uk/>) and the content of this paper for research or private study, educational, or not-for-profit purposes without prior permission or charge.

Any correspondence concerning this service should be sent to Strathprints administrator: strathprints@strath.ac.uk

2 **Evaluation of E.M. fields and energy transport in metallic**
3 **nanoparticles with near field excitation**

4
5
6
7
8 **ABSTRACT**
9

We compare two ways of calculating the optical response of metallic nanoparticles illuminated by near field dipole sources. We develop tests to determine the accuracy of the calculations of internal and scattered fields of metallic nanoparticles at the boundary of the particles and in the far field. We verify the correct transport of energy by checking that the evaluation of the energy flux agrees at the surface of the particles and in the far field. A new test is introduced to check that the surface fields fulfill Maxwell's equations allowing evaluation of the validity of the internal field. Calculations of the scattering cross section show a faster rate of convergence for the principal mode theory. We show that for metallic particles the internal field is the most significant source of error.

10
11 *Keywords: nanoparticles; electromagnetic scattering; energy flux; nanophotonics*
12

13 **1. INTRODUCTION**
14

15 Many of the recent developments in Nanophotonics imaging and sensing are based on the interaction of metallic particles
16 with sources of radiation located at sub wavelength distances from the particles [1]. The necessity to understand how to
17 optimize experimental set-ups and to extract the optical properties of the nanoparticles from the experimental results has
18 been a strong driver of the demand for accurate modeling of the interaction between incoming light and nanoparticles [2].
19 In Near Field Optical Microscopy in illumination mode one is interested in calculating the light originating from near field
20 interactions after it passes into the far field region, where the detector is placed [3]. For other forms of microscopy and for
21 surface enhanced spectroscopy and sensing, one needs to find the energy flux near the surface of the nanoparticles.
22 Because fully analytical calculations are possible only for the few shapes for which the Maxwell's equations admit
23 separation of variables, it is important to develop tests for assessing the ability of different methods to calculate quantities
24 of interest such as cross sections, field intensities and energy fluxes that have different convergence rates with respect to
25 computational parameters. Several efficient techniques have been developed to study scattering in non-spherical particles
26 [4-8]. In this paper we compare two implementations of the recently developed theory of the principal modes (TPM) for
27 internal and scattered fields [9-12], with the Discrete Sources Method (DSM) [13], which is very fast and able to calculate
28 the fields at any point in space. All these algorithms are able to treat non-spherical particles, and are based on the
29 decomposition of internal and scattered fields into sums of fields produced by electric and magnetic
30 multipoles distributed inside and/or outside the particles [13-15]. The principal mode theory is semi-analytical and based
31 on the decomposition of internal and external fields into orthogonal modes which are the generalization of Mie's solutions
32 [16] to non-spherical particles and whose amplitudes are found by projecting the incident fields on the modes themselves.
33 The explicit determinations of internal and scattering modes are used to find resonances [9] and develop control methods
34 [12]. On the contrary, the DSM determines the amplitude of internal and scattered multipoles by solving an overdetermined
35 system of equations. For these methods we compare the error in the boundary conditions at the surface and we find how
36 well these methods satisfy exact relations for the scattered energy flux and for internal and scattered fields.
37

38 **2. METHODOLOGY**
39

40 We compare the performances of TPM and DSM using the same number and distribution of electric and magnetic
41 multipoles inside and outside the particles and the same set of points on the surface of the particles. We have used a grid
42 of 8,000 points on the generatrix of the surface [10,17] for all the results shown in this paper and we have checked the
43 numerical convergence, see the discussion in the following section.

44 The internal and scattered fields excited by a given incident field are determined by satisfying the boundary conditions,

45
$$\hat{n}(p) \times \left(F^0(p) + \sum_{\nu=1}^m c_{\nu}^s F_{\nu}^s(p) \right) = \hat{n}(p) \times \sum_{\nu=1}^n c_{\nu}^i F_{\nu}^i(p), \quad (1)$$

where p is a point on the surface and \hat{n} is the unit vector normal to the surface, $F^0 = [E, H]^T$ is the incident field, $F_v^{i/s}$ are sets of v electric and magnetic multipoles summed to represent the internal and scattered fields, indexed i and s respectively, at that point. Sampling the multipoles on the generatrix of the surface leads to the $(m \times n)$ matrix L , where m is the number of sampling points and n the number of multipoles, which is the same starting point for all the methods used here. Gauss-Legendre quadrature points are used both for the sampling of the fields and also for surface integration along the generatrix line [10].

The DSM directly solves for the expansion coefficients of the multipoles, $c_v^{i/s}$, in a least squares sense typically by using Gaussian elimination. Alternatively the over-determined set of linear equations $Lx = f$ can also be solved by using the decomposition, $L = QR$, where Q is a square matrix whose columns are orthogonal and R is an upper triangular matrix [18]. The number of columns of Q is the rank of R , i.e. the dimension of the largest invertible minor of R . Theoretically the multipoles used are linearly independent, so Q should have n columns if using exact numerical precision. In practice, some of the multipoles give rise to columns of L that appear linearly dependent when using finite numerical precision; QR algorithms where the number of columns of Q are determined by a user defined upper bound on the ratio between the largest and the smallest eigenvalues (the estimated condition number) of R , are available [18]. The eigenvalues of R that would give rise to a poorer condition number are removed, and the corresponding columns of Q are eliminated. This procedure effectively reduces the number of the functions used to span the solution by eliminating the functions that are most affected by numerical noise.

The TPM method instead constructs n pairs of internal and scattered modes that are orthogonal on the surface, each consisting of a linear combination of the multipoles. This is achieved by considering submatrices $(m \times n_i) L_i$ and $(m \times n_s) L_s$ of L (i.e. $L = L_i + L_s$ and $n = n_i + n_s$) formed by sampling the internal and scattered modes, respectively. We then find internal and scattered orthonormal modes using either the decompositions $L_i = Q_i R_i$, $L_s = Q_s R_s$ or the singular value decompositions $L_i = U_i S_i V_i$, $L_s = U_s S_s V_s$. The matrices U_i , U_s , V_i , V_s are unitary and the matrices S_i , S_s are diagonal and positive. As with the QR decomposition, numerical noise can be reduced by setting the smallest terms in the matrices S_i , S_s to zero and eliminating the corresponding columns and rows of U_i , U_s and V_i , V_s . We then use the singular value decomposition of either $Q_i^\dagger Q_s$ or of $U_i^\dagger U_s$ to find the principal modes, i.e. two sets of internal and scattered modes that are correlated pairwise on the surface of the particle. For each incident field, the internal and scattered fields are found by projecting the incident fields on to the principal modes [9]. The amplitude of the n^{th} internal principal mode is obtained by using the expression,

$$a_n^i = \frac{i_n - (i_n \cdot s_n) s_n}{1 - (i_n \cdot s_n)^2} \cdot f^0. \quad (2)$$

Similarly the amplitudes of the modes in the scattered space can be obtained by changing the sign of Eqn. (2) and exchanging the sets of principal internal and scattered modes, i_n and s_n respectively, where the projection of the incident field is given by $f^0 = \hat{n} \times (\hat{n} \times F^0)$. Note that unlike the DSM, in the principal mode theory one can control separately the numerical solutions for the subspaces of the internal and scattering multipoles.

3. RESULTS AND DISCUSSION

We investigate the validity of the numerical solutions to the scattering problem calculated via three different methods; DSM using QR decomposition hereafter referred to as QR, TPM using solely Singular Value Decomposition (SVD) and also a TPM combination of both algorithms (QR+SVD). To provide a fair comparison between algorithms we limit the rank of the output for each method via regularization to be the same for all methods and study the effect of incrementing that limit. Simulations were run for two distinct particle types, a nanodisc of radius 400nm and depth 35nm and a nanorod of length 400nm and diameter 35nm, with rounded edges. Other than geometry, the two particles differ in the type of sources used to represent the fields. For the rod multipoles are distributed along the symmetry axis in the real space whereas for the disc the sources are located in the complex space effectively making them ring sources distributed concentrically along the particle radius [14]. The particles were illuminated by a near field source of wavelength 720nm

comprised of a combination of electric and magnetic point dipoles located 50nm from the particle surface. The approximate locations of the near field source, moved to obtain average values for some tests by using different locations and polarisations, are highlighted in Fig. 1.

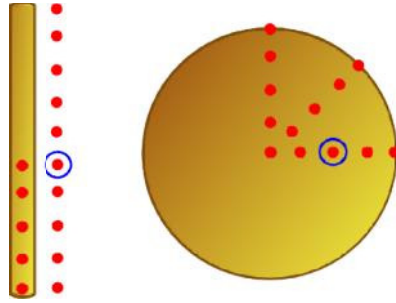


Fig. 1. Sampling points of near field excitation for a rounded gold nanodisc and nanorod. The red points indicate the approximate location of the near field source as it was scanned over the gold nanoparticles at a height of 50nm, for a rod with dimensions (l=400nm, d=35nm) and a disc (d=800nm, z=35nm). The blue circles indicate the location of the near field source for the differential scattering cross section and Stratton-Chu measurements. There are 15 sampling points for each particle (the centre of the disc was sampled with 3 different polarisations.) All of the following simulations were performed using these particles.

Firstly, we compare the convergence of the solutions by plotting the differential scattering cross sections (DSCS), the angular variation of the electric field intensity in the far field [13], of each of the three methods by increasing the rank from an effective minimum. These results were obtained by calculating the light scattered by the excited particles into the far field along the generatrix line, $\phi = 0$, sampling θ at equal intervals between the poles of the particle's symmetry axis at 0 and π , shown in Fig. 2. We observe that for minimal rank there is an obvious advantage to the TPM methods, which while not fully converged show the main features of the spectrum at the correct angles. The QR solution however, for both the rod and disc particles, fails to even approximately produce these features of the solution when the rank is minimal. As the rank is increased both TPM methods converge more rapidly than the pure QR solution which requires the maximum rank achievable with the TPM methods to show full convergence, for the disc, and approximate convergence for the rod. Note that with these particular source configurations the upper bound on the rank obtainable for SVD and QR+SVD when no limit is imposed is almost half that observed for the QR algorithm.

As we are solving the scattering problem by using a surface method we test the numerical validity of the surface fields primarily through the fractional L_2 surface error, where the norm of the surface field residual is calculated in terms of each input field [10],

$$\frac{|f^0 - f^i + f^s|^2}{|f^0|^2} \quad (3)$$

Where the tangential components of the incident, internal and scattered fields projected onto the particle surface are represented by f^0 , f^i , and f^s respectively. Due to the cylindrical symmetry of the particles we are able to separate components of the fields according to their angular phase dependence $\exp(im\phi)$, where m is the component of the optical angular momentum along the symmetry axis. Convergence of the fractional L_2 error test was checked with varying sized grids, ranging from 6000 to 12000 points, and a small oscillation of the computed value was observed but with a maximum deviation of ca. 6% of the results shown in Fig. 3. As we would expect from the results of the DSCS, SVD and QR+SVD perform much better with minimal rank and produce an acceptably small (less than 4%) L_2 error on the disc for $|m| \leq 2$, as shown in Fig. 3. As we increase the rank, we find that QR catches up with the TPM methods and that we have an error of less than 10% of the incident field for $|m| \leq 6$. Increasing the rank further for the pure QR case does produce an even lower L_2 error and it does begin to outperform the other methods at high $|m|$. The rod particle is much easier to integrate and we observe a very low residual up to $|m| = 7$ however due to the limited radius of the particle only the fields for $|m| \leq 2$ are non-negligible. For this type of particle, QR must retain a much higher rank of the composite matrices to perform as well as the TPM methods and so with limited rank the L_2 error fluctuates strongly as the near field source is scanned across the particle.

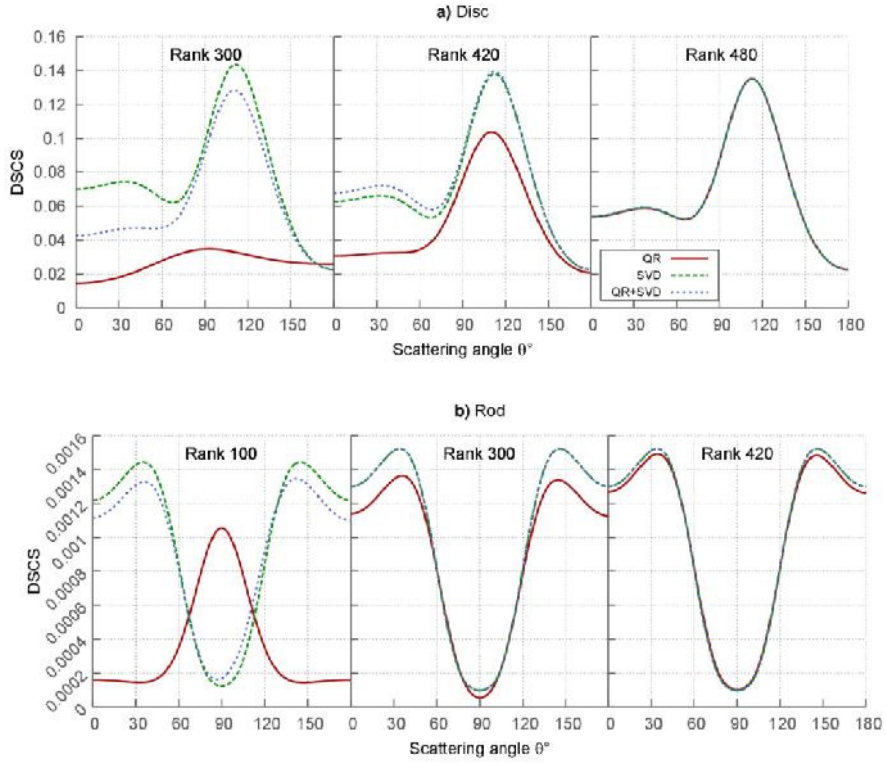


Fig. 2. Convergence of differential scattering cross sections (DSCS) along the generatrix line with increasing rank. The DSCS, in arbitrary units, for the three different algorithms plotted against the far field angle θ , varied incrementally between 0 and π between the poles of the particle's symmetry axis showing convergence with increasing rank of the solution matrices for a) disc and b) rod.

The error in the propagation of the scattered fields can be determined by comparing the integral of the Poynting vectors on the surface and also at infinity [13]. As with the L_2 error this test was checked for convergence by varying the number of grid points and the maximum deviation from the results reported in Fig. 3 was ca. 0.05%. This flux ratio gives an indication as to the quality of the scattered field produced by evaluating the error in the propagation of the special functions and for the disc particle all methods perform similarly despite the large difference in DSCS results and L_2 error, particularly with minimal rank. For the rod particle however, we only expect valid results from the flux ratio where the scattered field is non-negligible. Again, the QR method cannot compete with the TPM methods particularly with minimal rank however it does eventually perform as well when the rank is steadily increased beyond what is shown in Fig 3.

A further test of the validity of the calculated fields is the introduction of the Stratton-Chu test at infinity, where the scattered field can be compared with an exact solution of Maxwell's equations, and the Internal field should be exactly zero [13];

$$E_{S-C}(e_r) = \frac{ik_s}{4\pi} \int_S \left\{ e_r \times e_s(r') + \frac{e_r \times [h_s(r') \times e_r]}{C_s} \right\} e^{-ik_s e_r \cdot r'} dS(r') \quad e_r \in D_s \quad (4)$$

$$E_{S-C}(e_r) = 0 = \frac{ik_i}{4\pi} \int_S \left\{ e_r \times e_i(r') + \frac{e_r \times [h_i(r') \times e_r]}{C_i} \right\} e^{-ik_i e_r \cdot r'} dS(r') \quad e_r \in D_s \quad (5)$$

Here, E_{S-C} is the electric field calculated for a point at infinity, $k_{i/s}$ is the wavenumber in the internal and scattering media, the constant $C_{i/s} = \sqrt{\epsilon_{i/s} / \mu_{i/s}}$ where $\epsilon_{i/s}$ and $\mu_{i/s}$ are the relative permittivity and permeability in the internal and scattering media respectively, $e_{i/s}$ and $h_{i/s}$ are the tangential components of the surface electric and magnetic fields, e_r is the unit vector towards the evaluation point in the far field, r' is the point on the surface S and D_s is the scattering domain.

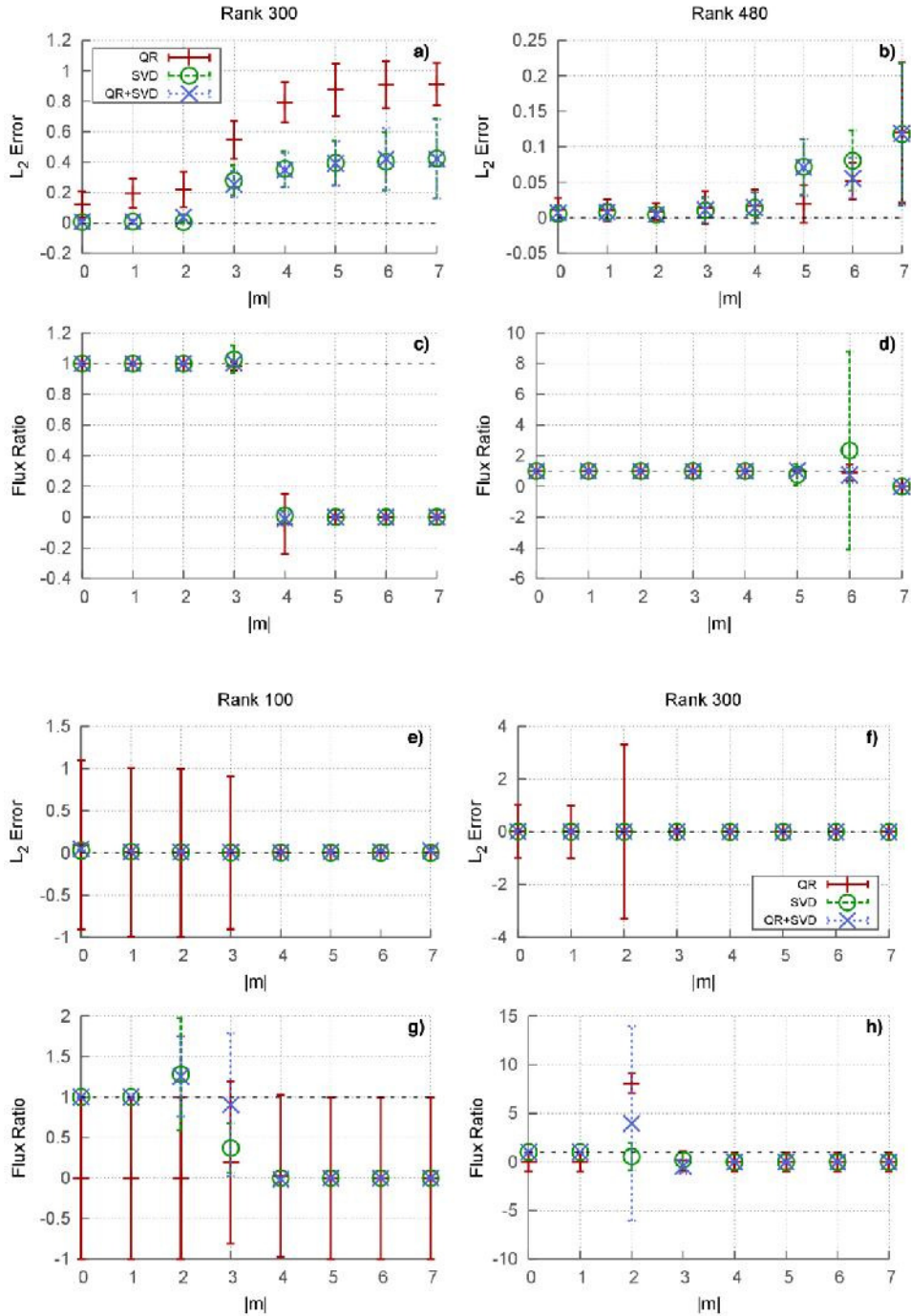


Fig. 3. Fractional L_2 surface error and flux ratio between the particle surface and the far field for a gold (a)-(d) nanodisc and (e)-(h) nanorod for the three solution methods plotted against the absolute value of the index of optical angular momentum, m , of the field. All points shown are the averages μ of the 15 sampling points indicated in Fig. 1 and the error bars show the

standard deviation $\sigma = \sqrt{1/(n-1) \sum_n (x_n - \mu)^2}$. The black dashed line indicates the ideal value in all plots.

We use the asymptotic form of the multipole sources [13], E_A , to evaluate the field calculated using from the scattered field as $(|E_A| - |E_{s-c}|)^2 / |E_A|^2$. The convergence of the Stratton-Chu test for the scattered field was again tested by varying the grid size and showed a maximum discrepancy of the order $1E-6$ when compared with the asymptotic values. A much larger fluctuation in results at wide angles was observed for the test of the internal field, which uses a different kernel to the scattered. In Fig. 4 we again see evidence that the disc particle is particularly difficult to integrate when

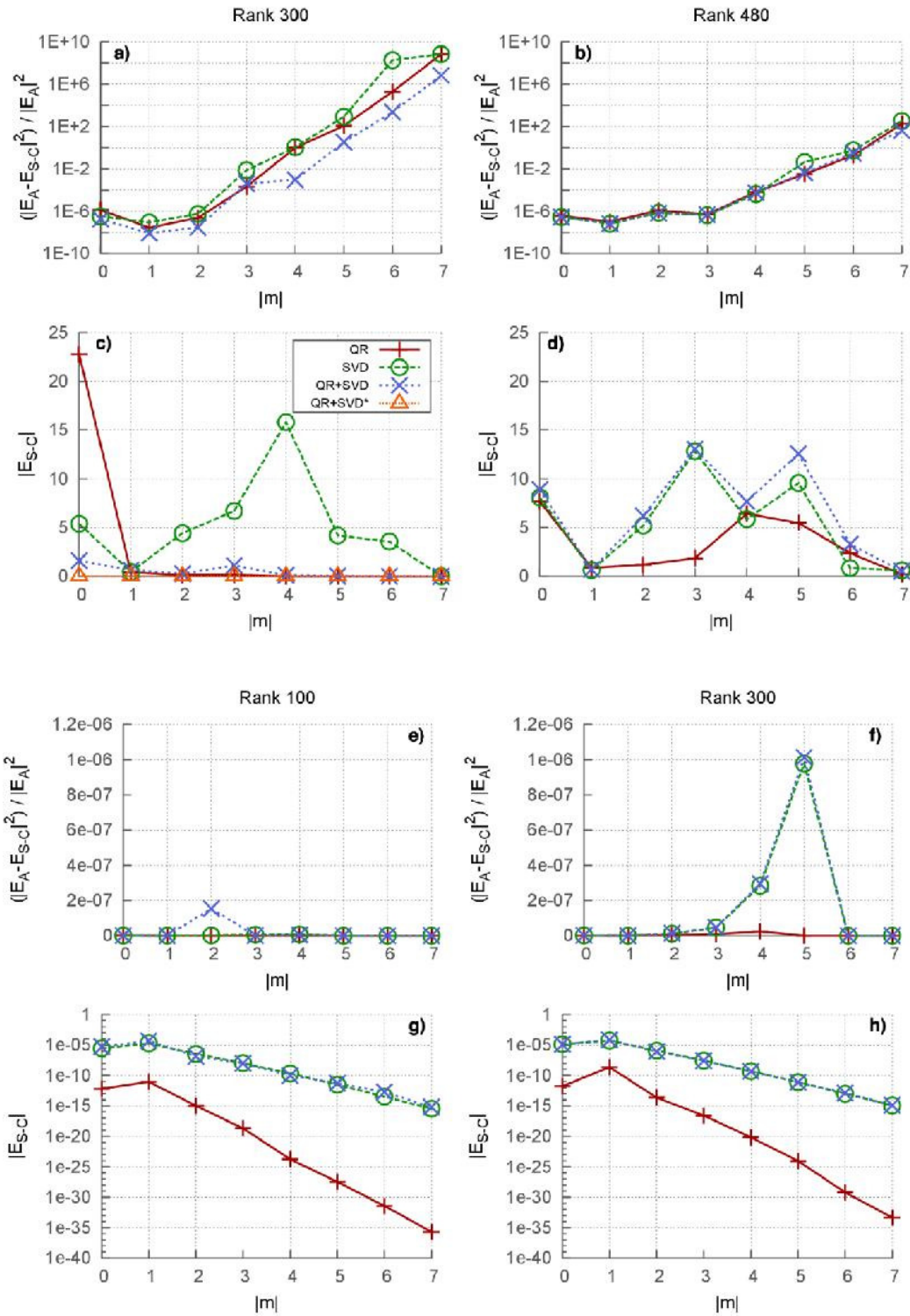
165 compared to the rod which gives excellent results over all the m channels for each method. For the disc only up to $|m| \leq 4$
 166 at low rank and $|m| \leq 6$ at higher rank give a value close to the value of the asymptotic sources for the scattered field, a
 167 result similar to that observed for the flux ratio. In fact the Stratton-Chu test proves to be a more stringent test of the
 168 scattered field than the flux ratio. The Stratton-Chu test on the internal field of the disc appears to indicate that there is a
 169 problem with the field. The field is evaluated along a line in the far field from zero to π , and is non-zero for wide angles
 170 around $\pi/2$. This is due to the fact that the grid along the curved edge of the particle is particularly difficult to integrate
 171 and has not converged for this number of grid points. To indicate this more clearly, in Fig. 4c we plot also the Stratton-Chu
 172 test for the internal field, calculated using QR+SVD on the surface of the disc, expanded out onto a sphere with radius
 173 equal to that of the disc, where it convincingly passes this test for all m channels at all angles. The QR algorithm appears
 174 to perform better for the internal field than the other methods but this is due to the fact that it assigns the sources
 175 significantly smaller amplitudes when solving for the fields at the particle boundary, as such the values calculated at
 176 infinity also appear smaller. To the best of our knowledge the Stratton-Chu test is the first procedure developed to
 177 evaluate the quality of the internal field.

178 We have observed that for low rank that there is a clear advantage to using a method which splits the space into two
 179 subspaces not only for the extra information about the system which is obtained but also for the accuracy in the
 180 calculations performed. There is also another advantage to using the TPM methods, due to the sequential way in which
 181 the surface fields are calculated using SVD they can be written out to be used again for a different excitation of the same
 182 particle. While, for the initial calculation QR proves to be slightly quicker, as shown in Table 1., for multiple calculations
 183 SVD and QR+SVD need only calculate the fields once and the subsequent calculations are significantly faster, by a factor
 184 of ~ 5 for QR+SVD and ~ 7 for SVD.

185 **Table 1. Total computational time for a full solution of the scattering problem for the disc particle using an AMD Opteron**
 186 **Processor 6344 2.6 GHz system averaged over 5 runs. For QR+SVD and pure SVD we highlight the time taken for the initial**
 187 **calculation and also subsequent calculations for the same particle where the fields are read back in.**

Algorithm	CPU time(s)
QR	509
SVD+SVD(initial)	1302
QR+SVD(initial)	972
SVD+SVD/QR+SVD(read)	182

188
 189



190

191 **Fig. 4. Evaluation of the internal and scattered fields using the Stratton-Chu test at infinity for the disc (a)-(d) and rod (e)-(h)**
 192 **particles. Plotted, for each of the three algorithms, are the average fields, E_{S-C} , calculated at 15 different points along θ from 0**
 193 **to $\pi, \varphi=0$ for different scattering channels m . The scattered fields are compared with exact solutions of the Maxwell equations**
 194 **E_A . Fig 4c) shows an additional plot, QR+SVD*, where the internal field calculated on the surface of the disc was expanded**
 195 **onto the surface of a sphere of equal radius**

196

197
198 **4. CONCLUSION**
199

200 In conclusion we have shown that the TPM - by separately considering the internal and scattered subspaces of the
201 electromagnetic fields - has a faster convergence with the number of functions used to expand these solutions than the
202 Discrete Source Method implemented through QR decomposition. In addition to evaluating the fractional error in the
203 calculated solutions at the particle surface, we have also quantitatively tested the quality of the numerical evaluation of the
204 transport of energy away from the particle. However this does not reveal errors in the field inside of the particle, hence we
205 have demonstrated that the Stratton-Chu relations offer an excellent metric for validating the reliability of both the internal
206 and scattered fields, providing the first general test for the internal field. For metallic particles these tests reveal that the
207 internal field is the most significant source of numerical error in these calculations. We have also shown that for particles
208 with large aspect ratio, such as those considered here, the accuracy of the surface quadrature is extremely important, this
209 suggests that integration via adaptive grids may be beneficial in improving the accuracy of the calculations.
210

211 **ACKNOWLEDGEMENTS**
212

213 D. McArthur acknowledges the EPSRC DTG for his studentship.

214 **COMPETING INTERESTS**
215

216 Authors have declared that no competing interests exist.
217
218

219 **REFERENCES**
220

221 [1] Kawata S. Near-field optics and surface plasmon polaritons. Berlin; New York: Springer; 2001

222 [2] Girard C, Dereux A. Rep Prog Phys. 1996;59,657: doi:10.1088/0034-4885/59/5/002

223 [3] Okamoto H, Imura K. J Phys Chem Lett. 2013;4(13):2230–2241

224 [4] Waterman PC. The T-matrix revisited. J Opt Soc Am A. 2007;24:2257–2267

225 [5] Barber P, Yeh C. Scattering of electromagnetic waves by arbitrarily shaped dielectric bodies. Appl Opt. 1975;14:2864–
227 2872

228 [6] Mishchenko MI, Hovenier JH, Travis LD, eds. Light Scattering by Nonspherical Particles: Theory, Measurements and
229 Applications. Academic Press; 2000

230 [7] Taflov A. Computational Electrodynamics: The Finite Difference Time-Domain Method. Boston: Artech House
231 Publishers; 1995

232 [8] Rodríguez-Oliveros R, Sánchez-Gil JA. Localized surface-plasmon resonances on single and coupled nanoparticles
233 through surface integral equations for flexible surfaces. Opt Express. 2011;19:12208–12219

234 [9] Papoff F, Hourahine B. Geometrical Mie theory for resonances in nanoparticles of any shape. Opt Express. 2011;19:
235 21432-21444

236 [10] Hourahine B, Holms K, Papoff F. Accurate light scattering for non spherical particles from Mie-type theory. J Phys.:
237 Conf Ser. 2012;367:012010

238 [11] Hourahine B, Papoff F. The geometrical nature of optical resonances: from a sphere to fused dimer
239 nanoparticles. Meas Sci Technol. 2012;23:084002

240 [12] Hourahine B, Papoff F. Optical control of scattering, absorption and line shape in nanoparticles. Opt Express.
241 2013;21:20322-20333

242 [13] Doicu A, Eremin Y, Wriedt T. Acoustic and electromagnetic scattering analysis using discrete sources. New York:
243 Academic Press; 2000

- 248 [14] Doicu A, Wriedt T. Extended boundary condition method with multipole sources located in the complex plane. Opt
249 Comm. 1997;139:85-91
- 250 [15] Borghese F, Denti P, Saija R. Scattering from model non-spherical particles: Theory and applications to
251 environmental physics. second edition. Berlin; Springer-Verlag. 2007
- 252 [16] Mie G. Leipzig Ann Phys. 1908;330:377-445 German.
- 253 [17] Holms K, Hourahine B, Papoff F. Calculation of internal and scattered fields of axisymmetric nanoparticles at any
254 point in space. Jour Opt A. 2009;11:054009
- 255 [18] Golub GH, van Van Loan CF. Chapter 5: Matrix Computations. Johns Hopkins University Press. 2nd ed. 1990